CAPOS: the bulge Cluster APOgee Survey
II. The Intriguing "Sequoia" Globular Cluster FSR 1758

María Romero-Colmenares[1,2]*, José G. Fernández-Trincado[2]**, Doug Geisler[3,4,5], Stefano O. Souza[6], Sandro Villanova[3], Penélope Longa-Peña[1], Dante Minniti[7,8], Timothy C. Beers[9], Cristian Moni Bidin[10], Angeles Pérez-Villegas[11], Edmundo Moreno[12], Elisa R. Garro[7], Ian Baeza[3], Lady Henao[3], Beatriz Barbuy[6], Javier Alonso-García[1,13], Roger E. Cohen[14], Richard R. Lane[2], and Cesar Muñoz[4,5]

(Affiliations can be found after the references)

ABSTRACT

We present results from a study of fifteen red giant members of the intermediate-metallicity globular cluster (GC) FSR 1758 using high-resolution near-infrared spectra collected with the Apache Point Observatory Galactic Evolution Experiment II survey (APOGEE-2), obtained as part of CAPOS (the bulge Cluster APOgee Survey). Since its very recent discovery as a massive GC in the bulge region, evoking the name Sequoia, this has been an intriguing object with a highly debated origin, and initially led to the suggestion of a purported progenitor dwarf galaxy of the same name. In this work, we use new spectroscopic and astrometric data to provide additional clues to the nature of FSR 1758. Our study confirms the GC nature of FSR 1758, and as such we report for the first time the existence of the characteristic N-C anti-correlation and Al-N correlation, revealing the existence of the multiple-population phenomenon, similar to that observed in virtually all GCs. Furthermore, the presence of a population with strongly enriched aluminium makes it unlikely FSR 1758 is the remnant nucleus of a dwarf galaxy, as Al-enhanced stars are uncommon in dwarf galaxies. We find that FSR 1758 is slightly more metal rich than previously reported in the literature, with a mean metallicity [Fe/H] between -1.43 to -1.36 (depending on the adopted atmospheric parameters), and with a scatter within observational error, again pointing to its GC nature. Overall, the α-enrichment ($\gtrsim +0.3$ dex), Fe-peak (Fe, Ni), light- (C, N), and odd-Z (Al) elements follow the trend of intermediate-metallicity GCs. Isochrone fitting in the *Gaia* bands yields an estimated age of ~ 11.6 Gyr. We use the exquisite kinematic data, including our CAPOS radial velocities and *Gaia* eDR3 proper motions, to constrain the *N*-body density profile of FSR 1758, and found that it is as massive ($\sim 2.9 \pm 0.6 \times 10^5$ $M_\odot$) as NGC 6752. We confirm a retrograde and eccentric orbit for FSR 1758. A new examination of its dynamical properties with the `GravPot16` model favors an association with the Gaia-Enceladus-Sausage accretion event. Thus, paradoxically, the cluster that gave rise to the name of the Sequoia dwarf galaxy does not appear to belong to this specific merging event.

Key words. Stars: abundances – Stars: chemically peculiar – Galaxy: globular clusters: individual: FSR 1758 – Techniques: spectroscopic

1. Introduction

The bulge of the Milky Way (MW) is populated by a large collection ($\gtrsim 40$) of ancient globular clusters (GCs) within ~ 3.5 kpc of the Galactic center (for a detailed description, see a review by Bica et al. 2016; Barbuy et al. 2018; Pérez-Villegas et al. 2020), which serves as the 'fossil record' of its evolutionary history (Recio-Blanco et al. 2017; Minniti et al. 2018a; Kundu et al. 2019, 2021; Fernández-Trincado et al. 2019a,b, 2020a,c,e, 2021a, 2020b, 2021b; Minniti et al. 2021, Minniti2021a).

However, until very recently only a very small number of them have been studied with sufficient detail, including uncovering the multiple-population phenomenon (Côté 1999; Minniti 1995; Mészáros et al. 2020; Fernández-Trincado et al. 2019c, 2020f, 2021a,c; Geisler et al. 2021, and references therein). Due to the high and variable extinction produced by the large amount of dust present in the Galactic plane, which highly hampers optical observations, most of these GCs have remained barely explored.

More recently, with the aid of near-infrared (NIR) photometric and high-resolution spectroscopic instruments, capable of penetrating the obscuring dust, several modern surveys have allowed us to overcome these limitations and begin to explore and scientifically exploit these fascinating objects. The *Vista Variables in the Via Lactea survey* (VVV: Minniti et al. 2010; Saito et al. 2012; Alonso-García et al. 2018), and its eXtension (VVVX: Minniti et al. 2018b) is a key large-scale NIR photometric survey of the bulge and the surrounding disk.

In addition to providing deep NIR photometry for all known bulge GCs, VVV/VVVX has revealed that the GC census toward the Galactic bulge is incomplete, and more than 100 new low-luminosity GC candidates have been discovered in the bulge area (Minniti et al. 2017a,b,c, 2018c; Ryu & Lee 2018; Bica et al. 2018; Contreras Ramos et al. 2018; Camargo 2018; Camargo & Minniti 2019; Minniti et al. 2019; Gran et al. 2019; Palma et al. 2019; Minniti et al. 2020; Garro et al. 2021), and toward the Sagittarius dwarf galaxy (see, e.g., Minniti et al. 2021).

Complementarily, large spectroscopic surveys such as the Apache Point Observatory Galactic Evolution Experiment (APOGEE; Majewski et al. 2017) reveal detailed information about the chemical properties of obscured GCs for a number of species with a variety of nucleosynthetic origins with high precision (<0.05 dex). Fortunately, APOGEE has helped fill in the missing link of bulge GC abundances and velocities. However,

---

Table 1. Photometric, kinematic, and astrometric properties of fifteen likely members of FSR 1758.

APOGEE-ID	α hh:mm:ss	δ dd:mm:ss	J	H	K_s	$(G_{BP} - G_{RP})_0$	G_0	RV km s^{-1}	$\mu_\alpha \cos(\delta)$ mas yr^{-1}	μ_δ mas yr^{-1}
S/N > 60										
2M17314970−3956247	17:31:49.71	−39:56:24.8	10.60	9.57	9.31	2.51	13.61	220.9	−2.994± 0.028	2.511±0.019
2M17305424−3950496	17:30:54.24	−39:50:49.6	11.13	10.19	9.93	2.42	14.04	227.7	−3.005± 0.027	2.489±0.021
2M17310731−3953523	17:31:07.32	−39:53:52.4	11.74	10.82	10.58	2.35	14.69	224.5	−2.863± 0.035	2.526±0.023
2M17310187−3950066	17:31:01.88	−39:50:06.7	12.07	11.19	10.91	2.36	14.97	228.6	−2.895± 0.039	2.477±0.029
2M17314263−3947053	17:31:42.64	−39:47:05.4	12.18	11.35	11.16	2.24	14.91	220.7	−2.983± 0.039	2.529±0.030
2M17312661−3951342	17:31:26.62	−39:51:34.3	12.20	11.48	11.24	2.31	15.29	226.3	−2.769± 0.040	2.584±0.028
2M17310738−3952298	17:31:07.39	−39:52:29.9	12.50	11.65	11.35	2.24	15.20	228.2	−2.850± 0.048	2.405±0.033
2M17311707−3950382	17:31:17.07	−39:50:38.2	12.73	11.91	11.70	2.20	15.54	226.4	−2.863± 0.049	2.392±0.034
2M17313165−3949120	17:31:31.65	−39:49:12.1	12.85	12.11	11.92	2.03	15.43	220.2	−2.863± 0.050	2.690±0.035
2M17311230−3949493	17:31:12.31	−39:49:49.4	11.90	11.06	10.75	2.29	14.91	223.4	−2.619± 0.038	2.713±0.026
2M17310618−3943037	17:31:06.18	−39:43:03.8	13.25	12.48	12.23	2.14	15.92	225.0	−2.777± 0.053	2.526±0.041
S/N < 60										
2M17304430−3952504	17:30:44.31	−39:52:50.5	12.62	11.86	11.67	2.11	15.27	225.5	−2.729± 0.041	2.573±0.029
2M17310004−3954546	17:31:00.04	−39:54:54.7	13.21	12.43	12.24	1.96	15.64	225.7	−2.774± 0.055	2.506±0.041
2M17312078−3948416	17:31:20.79	−39:48:41.7	13.16	12.35	12.20	2.00	15.74	225.9	−2.836± 0.057	2.529±0.043
2M17305633−3953349	17:30:56.34	−39:53:35.0	13.09	12.39	12.16	2.08	15.78	222.2	−2.832± 0.050	2.367±0.038

despite the large number of SDSS-IV bulge fields, the Survey only observed a handful of bulge GCs. Masseron et al. (2019), Mészáros et al. (2020) and Mészáros et al. (2021) present the first homogeneous study of the SDSS-IV sample of 44 GCs, of which only 2 are bona fide Main Bulge GCs according to Massari et al. (2019) and have a large enough sample of well-observed members and low enough reddening for their study. This is <4% of the total number of bulge GCs known, a disconcertingly low value. In order to take full advantage of the wealth of astrophysical detail these key objects can provide, as complete a sample as possible is essential.

Hence the CAPOS project, the bulge Cluster APOgee Survey (Geisler et al. 2021). The primary goal of CAPOS is to obtain detailed abundances and kinematics for as complete a sample as possible of bona fide members in bulge GCs, using the unique advantages of APOGEE in order to complement the small sample observed by SDSS-IV.

One of the CAPOS targets is FSR 1758. It was originally catalogued as a diffuse open cluster by Froebrich et al. (2007) and Kharchenko et al. (2013). Recently, Cantat-Gaudin et al. (2018) and Barbá et al. (2019) re-discovered this object using a combination of data from the DECam Plane Survey (DECaPS; Schlafly et al. 2018) and the VVVX survey, complemented with *Gaia* DR2 (see Gaia Collaboration et al. 2018a). The latter study revealed that the cluster motion is very different from nearby field stars.

Presumably located on the far side of the Galactic bulge region from the Sun at ~11.5±1.0 kpc (Barbá et al. 2019), FSR 1758 is as large (with a tidal radius ~150 pc) as ω Cen and NGC 2419, with possibly some signatures of extra-tidal features. The GC lies in a region strongly affected by the large foreground reddening, with E(B−V)> 0.7 mags (this work), even larger than the value previously estimated, E(B−V)~0.37, in Barbá et al. (2019). In their re-discovery paper, Barbá et al. (2019) posited that FSR 1758 could be the central part of a defunct dwarf galaxy, based on a possible halo of common proper motion stars in the surrounding regions of the cluster, or instead an unusually large GC.

However, a subsequent spectroscopic study in the optical (Villanova et al. 2019) revealed that FSR 1758 displays no significant intrinsic metallicity spread (~0.08 dex, within the observational errors) and also only a small velocity dispersion (< 5 km s^{-1}). In addition, it also possesses a Na-O anti-correlation similar to those seen in other GCs at similar metallicity. Moreover, it is now believed that the putative extratidal stars found by Barbá et al. (2019) were simply outliers in the surrounding field star proper motion distribution and likely not associated with the GC. All of this evidence supports the genuine GC nature of FSR 1758, and not the hypothesis that this is the remnant nucleus of a dwarf galaxy. However, the dynamical properties of FSR 1758 reveal that it is not a cluster that originated in the inner Galaxy, and on the contrary is a halo intruder which circulates throughout the bulge in a highly eccentric, radial, and retrograde orbital configuration (see, e.g., Simpson 2019; Villanova et al. 2019; Yeh et al. 2020).

Regarding its origin, several different scenarios have been proposed for FSR 1758. Simpson (2019), based on its retrograde orbit, claimed that it could be an accreted halo GC; Villanova et al. (2019) argued that it is a genuine MW GC based on the above evidence; and Yeh et al. (2020) also supports the idea that it is likely a halo GC formed inside the MW, as the highly eccentric and retrograde orbital configuration are not uncommon among *in situ* halo GCs (Massari et al. 2019). On the other hand, Myeong et al. (2019) suggested that it belongs to the remnant debris of an early accretion event in the Milky Way, likely associated with a massive dwarf galaxy, similar to accretion events suggested for other GCs (see, e.g., Myeong et al. 2019; Kruijssen et al. 2019). Myeong et al. (2019) coined the name Sequoia for the putative progenitor dwarf, based on the description of FSR 1758 as a "Sequoia in the garden" given in the title of the paper by Barbá et al. (2019). Subsequent work (Massari et al. 2019; Koppelman et al. 2019; Fernández-Trincado et al. 2019a, 2020a) have shown that indeed such an event occurred, with clear kinematic and chemical evolution signatures, and the name Sequoia has stuck for the progenitor. What is not clear, and one of the issues we will address here, is whether or not this
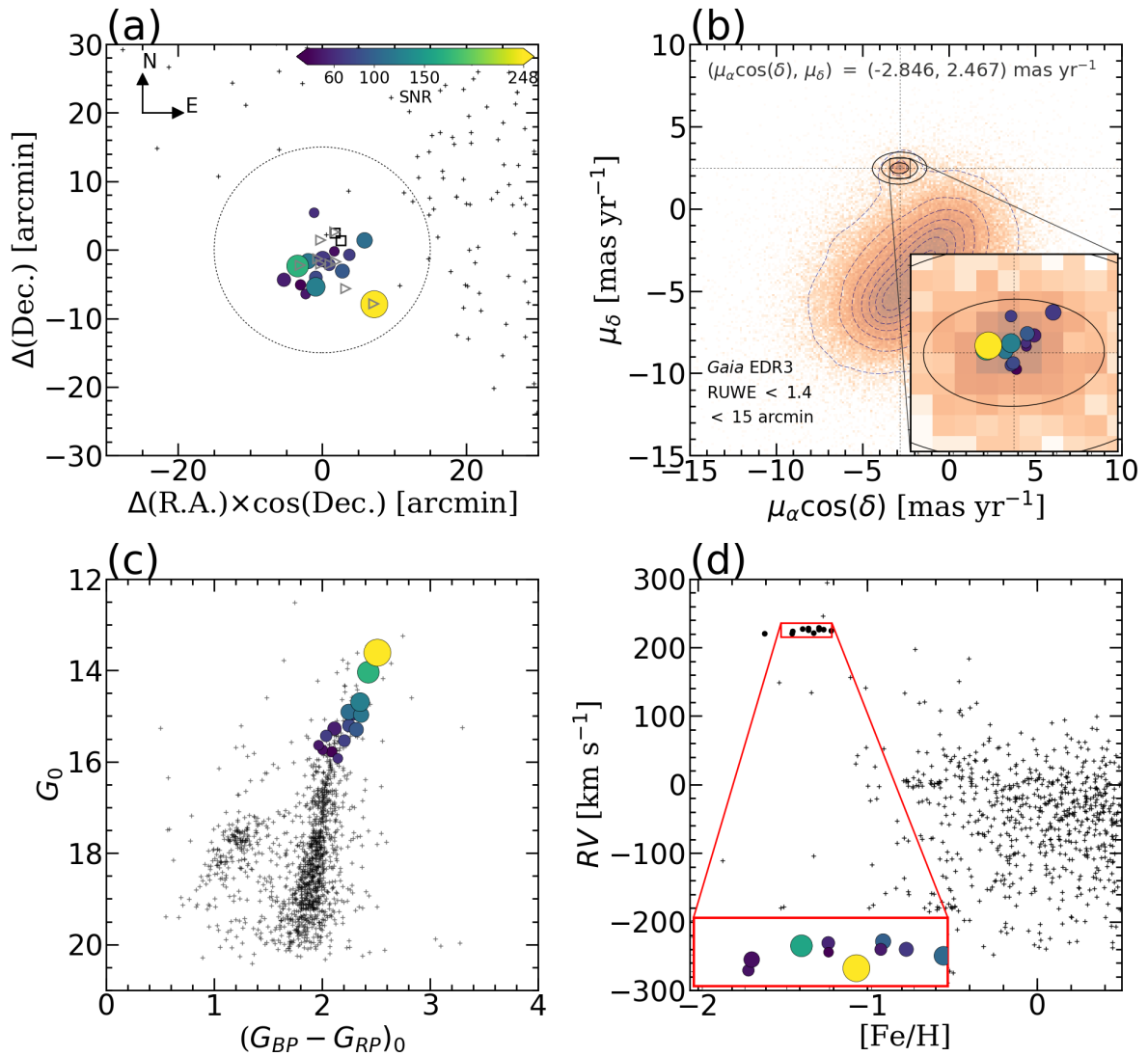
Fig. 1. Properties of our FSR 1758 targets. Panel (a): Spatial position. Colour-coded symbols represent the SNR of stars with APOGEE spectra whose sizes are proportional to their G mag. Open black squares and grey triangles are stars analyzed in Simpson (2019) and Villanova et al. (2019), respectively. Field stars are black crosses. A circle with 15′ radius is overplotted. Panel (b): The proper motion density distribution of stars located within 15′ from the cluster center, with color contours refering to the Kernel Density Estimation of this sample. FSR 1758 is clearly distinguishable from the field population. The inner plot on the top-right shows a zoom-in of the cluster, with concentric ellipses showing the 1, 2, and 3σ levels of our best fit proper motions of FSR 1758 based on *Gaia* EDR3 data, whose mean values are highlighted. Symbols are the same as in panel (a). Panel (c): Colour-magnitude diagram corrected by differential reddening and extinction-corrected in the *Gaia* bands of our sample and stars within 15′. Our targets all lie along the red giant branch. Panel (d): Radial velocity versus metallicity of our members compared to field stars. The [Fe/H] of our targets have been determined with BACCHUS and photometric atmospheric parameters (see Table 2), while the [Fe/H] of field stars are from the ASPCAP pipeline. The red box limited by ±0.15 dex and ±10 km s^{-1} and centered on [Fe/H]= −1.36 and RV = 225.73 km s^{-1} encloses our potential cluster members.

eponymous GC is indeed a member of the Sequoia dwarf. We in fact show that it was likely not a member.

In this work, we take advantage of data from the CAPOS survey (Geisler et al. 2021) to examine, for the first time in the *H*-band, the chemical and kinematic properties of FSR 1758, clarifying the characteristics of this interesting object in the dense inner regions of the MW, in particular its origin. This paper represents the second in the series on CAPOS data. In Section 2, we describe the data. In Section 3, the potential cluster mem-

bers are presented. In Section 4, we describe the adoption of the atmospheric parameters. In Section 5, the elemental-abundance determinations are highlighted. In Section 6, we present our estimation of the age of the cluster by adopting a Bayesian approach, while in Section 7, we provide a mass estimation of FSR 1758 based in the available kinematic data. In Section 8, the origin of FSR 1758 is examined from a dynamical point of view. Summary and concluding remarks are presented in Section 9.
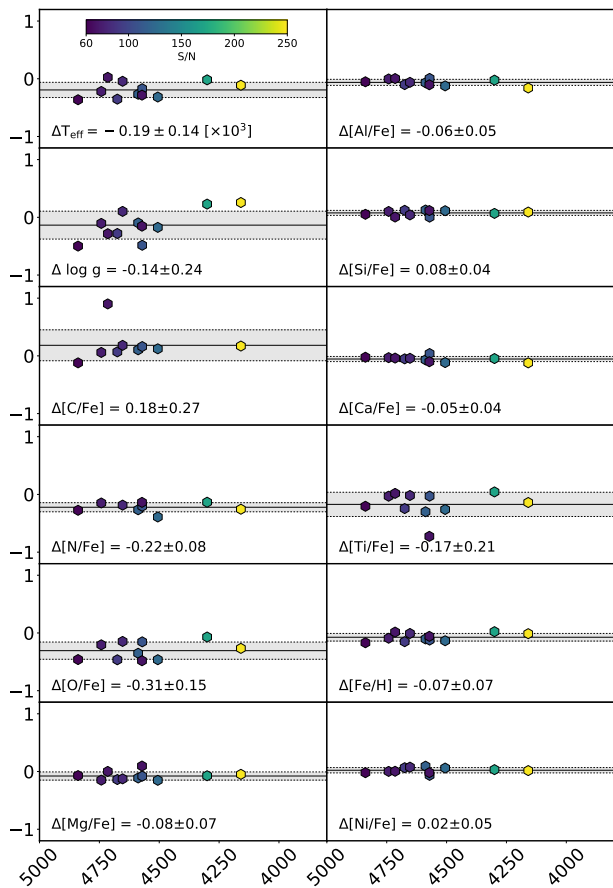
Fig. 2. Differences in atmospheric parameters and elemental abundances produced by two runs adopting different effective temperatures (T_{eff}) and surface gravities (log g): photometric versus spectroscopic values as listed in Table 2. The vertical axis refer to the Δ of every atmospheric parameter and chemical specie ([X/Fe]) analyzed in this work. The horizontal axis refer to the $T_{eff}^{photometry}$. The hexagonal symbols are color-coded by the S/N. The average and standard deviation around the mean of the differences is listed in each panel, and are marked by a black line and gray shadow.

2. Data and sample

The Apache Point Observatory Galactic Evolution Experiment II survey (APOGEE-2; Majewski et al. 2017) is one of the internal programs of the Sloan Digital Sky Survey-IV (Blanton et al. 2017; Ahumada et al. 2020) developed to provide precise radial velocities (RV <1 km s^{-1}) and detailed chemical abundances for an unprecedented large sample of giant stars, aiming to unveil the dynamical structure and chemical history of the entire MW galaxy.

The APOGEE-2 instruments (capable of observing up to 300 objects simultaneously) are high-resolution ($R \sim 22,500$), near-infrared (NIR) spectrographs (Wilson et al. 2019) observing all the components of the MW (halo, disc, and bulge) from the Northern Hemisphere on the 2.5m telescope at Apache Point Observatory (APO, APOGEE-2N; Gunn et al. 2006) and the Southern Hemisphere on the Irénée du Pont 2.5m telescope (Bowen & Vaughan 1973) at Las Campanas Observatory (LCO, APOGEE-2S). Each instrument records most of the H-band ($1.51\mu m$ – $1.69\mu m$) on three detectors, with coverage gaps between ∼1.58–1.59μm and ∼1.64–1.65μm, and with each fiber subtending a
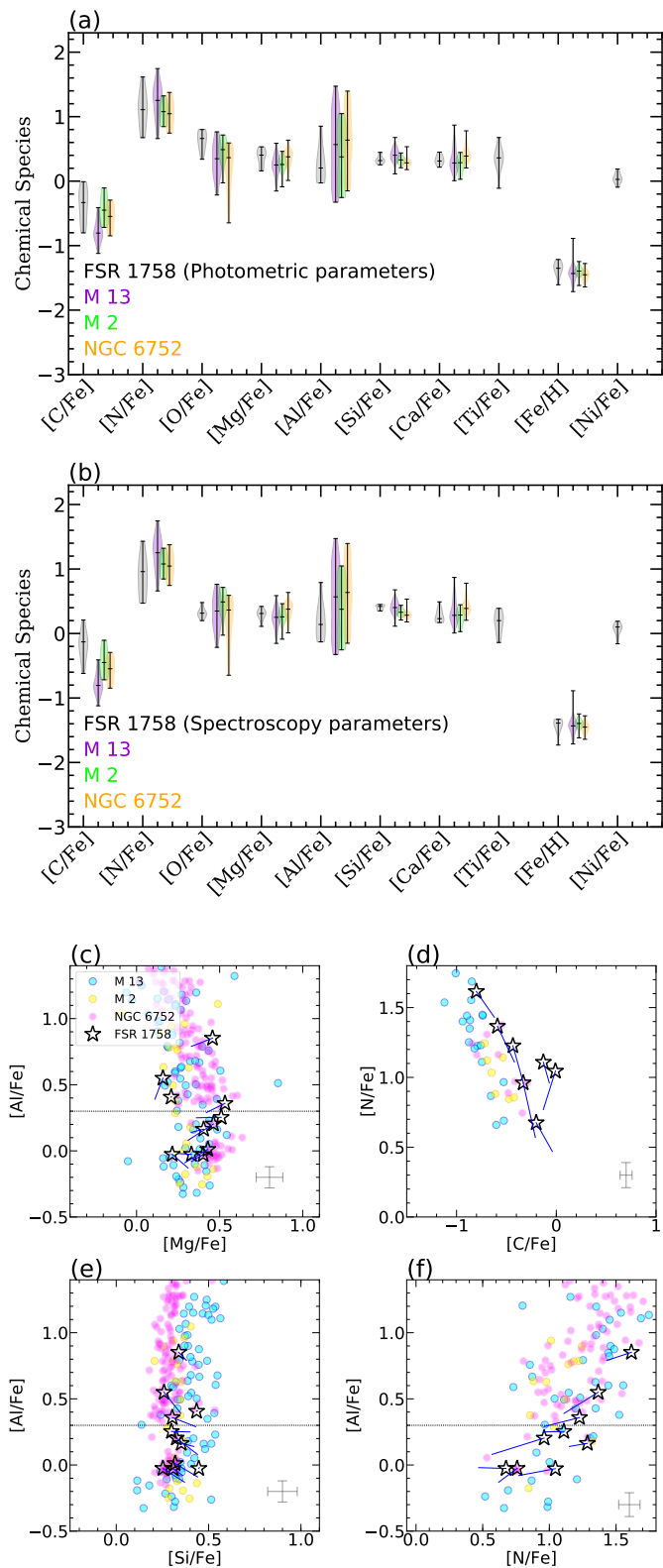
Fig. 3. Elemental abundances. [X/Fe] and [Fe/H] abundance density estimation (violin representation) of FSR 1758 (black) compared to Galactic GCs at similar metallicity from Mészáros et al. (2020). Panels (a) and (b) show our determinations by adopting photometric atmospheric parameters from photometry and spectroscopy (see Table 2), respectively. Each violin representation indicates with vertical lines the median and limits of the distribution. (c)–(f): [Al/Fe] – [Mg/Fe], [N/Fe] – [C/Fe], [Al/Fe]–[Si/Fe], and [Al/Fe]–[N/Fe] distributions for GCs from Mészáros et al. (2020) at similar metallicity. The black dotted line at [Al/Fe] = +0.3 denotes the generalized separation of first- and second-generation stars as envisioned by Mészáros et al. (2020). FSR 1758 stars shown 'star' symbols refers to our determinations with adopted photometry parameters, while the blue lines show the corresponding position of [X/Fe] determined from spectroscopic paramters. The typical internal error bars are also shown.

~2" diameter on-sky field of view in the northern instrument and 1.3" in the southern.

DR 17 is the final release of APOGEE-2 data from SDSS-III/SDSS-IV. We used our access to the internal version of DR 17, as the public version is not yet available. It includes all APOGEE data, including data taken at APO through November 2020 and at LCO through January 2021. The dual APOGEE-2 instruments have observed more than $650,000$ stars throughout the MW, targeting these objects with selections detailed in Zasowski et al. (2017), Santana et al. (2021) and Beaton et al. (2021). These papers also give a detailed overview of the targeting strategy of the APOGEE-2 survey. Spectra are reduced as described in Nidever et al. (2015), and analyzed using the APOGEE Stellar Parameters and Chemical Abundance Pipeline (ASPCAP; García Pérez et al. 2016), and the libraries of synthetic spectra described in Zamora et al. (2015). The accuracy and precision of the atmospheric parameters and chemical abundances are extensively analyzed in Holtzman et al. (2018), Jönsson et al. (2018), and Jönsson et al. (2020), while details regarding the customised H-band line list are fully described in Shetrone et al. (2015), Hasselquist et al. (2016), Cunha et al. (2017), and Smith et al. (2021).

3. FSR 1758

The GC FSR 1758 was observed as part of the Contributed APOGEE-2S CNTAC[1] CN2019A−98 program (P.I: Doug Geisler) during July 9–10, 2019 as part of the CAPOS survey (Geisler et al. 2021).

3.1. Proper motion selection

The APOGEE-2S plug-plate containing the FSR 1758 cluster was centered on $(l,b) \sim (350, -3.0)$, and 21 of 264 science fibers were located inside a radius of ≤ 15′from the cluster center, as shown in Figure 1(a). Targets were selected on the basis of *Gaia* DR2 (Gaia Collaboration et al. 2018a) proper motions within a radius of ~0.7 mas yr^{-1} around the nominal PMs of FSR 1758 computed by Villanova et al. (2019) from *Gaia* DR2:$\mu_\alpha \cos(\delta) = -2.79 \pm 0.01$ mas yr^{-1} and $\mu_\delta = 2.60 \pm 0.01$ mas yr^{-1}. However, here we re-examine these values taking advantage of the improved data from *Gaia* EDR3 (Gaia Collaboration et al. 2021). Thus, Figure 1(b) shows an updated version of the PMs using *Gaia* EDR3, which shows that only 15 out of the 21 originally observed "cluster" stars share PMs similar to the nominal PMs of FSR 1758, making them likely cluster members.

As in Villanova et al. (2019), we furthermore took potential cluster members within 15 ′ with *Gaia* EDR3 information, and having a Renormalised Unit Weight Error, RUWE ≤ 1.4 (Lindegren et al. 2018), in order to ensure that the selected stars were astrometrically well-behaved. Cluster members were also selected within an approximate radius of 1.0 mas yr^{-1} as an initial guess for proper motion members in order to remove field contamination from the colour-magnitude diagram (CMD). We fit one to ten Gaussians to the distribution of $\mu_\alpha \cos(\delta)$ and μ_δ with a Gaussian Mixture Model (GMM), and measured the Akaike Information Criterion (AIC) (Akaike 1974) and the Bayesian Information Criterion (BIC) (Schwarz 1978). Using these criteria, we then apply a GMM with only one Gaussian as this number minimized both the AIC and BIC, indicating it was the best fit. The two PM components of FSR 1758 in Gaia

---

[1] Chilean National Telescope Allocation Committee

EDR3 are found to have $\mu_\alpha \cos(\delta) = -2.85 \pm 0.05$ mas yr^{-1} and $\mu_\delta = 2.47 \pm 0.05$ mas yr^{-1}–as indicated by black dashed lines in Figure 1(b), which are similar to the previously estimated value from Villanova et al. (2019), and in excellent agreement with the nominal values reported in Vasiliev & Baumgardt (2021), $\mu_\alpha \cos(\delta) = -2.880 \pm 0.026$ mas yr^{-1} and $\mu_\delta = 2.519 \pm 0.025$ mas yr^{-1}.

Aside from PMs, stars in our sample are positioned close to the tip of the red giant branch (RGB), as shown in the *Gaia* EDR3 CMD in Figure 1(c). All selected stars had 2MASS H-band brighter than 12.5. This was required in order to achieve a nominal minimal signal-to-noise, S/N ≳60 pixel^{-1}, in one plug-plate visit (~ 1 hour). Although more visits were originally planned, in the end, given weather and time allocation and airmass constraints, only 1 visit was indeed obtained. Eleven out of the fifteen observed stars reached S/N> 60 pixel^{-1}, while the remaining spectra have lower S/N, ranging from 33 to 51. In the following, we use all stars to provide reliable and precise (< 1 km s^{-1}) radial velocities for cluster member confirmation, but limit ourselves to the 11 higher S/N stars for the abundance analysis, which are highlighted in Figure 1(d).

3.2. Photometric selection

The CMD presented in Figure 1(c) was differential reddening-corrected by using giant stars, and adopting the reddening law of Cardelli et al. (1989) and O'Donnell (1994) and a total-to-selective absorption ratio $R_V = 3.1$. For this purpose, we selected all RGB stars within a radius of 15 ′ from the cluster center and that have proper motions compatible with that of FSR 1758 within 1 mas yr^{-1}. First, we draw a ridge line along the RGB, and for each of the selected RGB stars we calculated its distance from this line along the reddening vector. The vertical projection of this distance gives the differential A_G absorption at the position of the star, while the horizontal projection gives the differential $E(G_{BP} - G_{RP})$ reddening at the position of the star. After this first step, for each star of the field we selected the three nearest RGB stars, calculated the mean differential A_G absorption and the mean differential $E(G_{BP} - G_{RP})$ reddening, and finally subtracted these mean values from its $G_{BP} - G_{RP}$ colour and G magnitude. We underline the fact that the number of reference stars used for the reddening correction is a compromise between having a correction affected as little as possible by photometric random error and the highest possible spatial resolution.

3.3. Spectroscopic selection

Figure 1(d) reveals the BACCHUS [Fe/H] abundance ratios versus the radial velocity of our eleven potential cluster members compared to field stars with ASPCAP/APOGEE-2 [Fe/H] determinations, which have been shifted by + 0.11 dex in order to minimize the systematic differences between ASPCAP/APOGEE-2 and BACCHUS, as highlighted in Appendix D in Fernández-Trincado et al. (2020d). First, we note that all of our targets have very similar velocities which are extreme compared to the field star distribution. This again points to the very strong likelihood of cluster membership for all of our targets. We find a mean RV from 15 APOGEE-2 stars of +224.9± 0.7 km s^{-1}, which is in good agreement with Simpson (2019), $RV = +227 \pm 1$ km s^{-1}, and Villanova et al. (2019), $RV = +226.8 \pm 1.6$. Other apparent sources inside this box are fore-/background stars with properties do not compatible with the cluster.

The red box highlighted in Figure 1(d) encloses the cluster members within ±0.15 dex and ±10 km s⁻¹ from the nominal mean [Fe/H]= −1.36 dex and *RV*= +225.73 km s⁻¹ of FSR 1758, as determined in this work (see Section 7). Note that one of our stars, 2M17314263−3947053, exhibits an [Fe/H] of −1.61, which is $\gtrsim 3\sigma$ more metal poor than the mean metallicity of the other members. For this particular case, the low-metallicity effect could be attributed to variability signature in this star (see, e.g., Muñoz et al. 2018, for instance), but its confirmation is beyond the scope this work. However, given the similarity of this star in *RV* and PM to the kinematics/astrometry of the other stars, we consider that this is indeed a member with an outlying metallicity value.

Table 1 lists the 2MASS photometry, the differential reddening corrected *Gaia* photometry, and the main astrometric and kinematic properties of the observed FSR 1758 stars.

4. Atmospheric parameters

4.1. The BACCHUS code

Since the method of deriving stellar parameters and elemental abundances is identical to that as described in Fernández-Trincado et al. (2019b) and Fernández-Trincado et al. (2019a), here we provide only a short overview of it. We adopted the un-calibrated T_{eff} and log g, and as a first guess the uncalibrated overall metallicity, as computed by the ASPCAP pipeline. Secondly, we made a careful inspection of each spectrum with the BACCHUS code to re-derive the metallicity, broadening parameters, and chemical abundances, based on a simple line-by-line approach. The abundance determination uses the BACCHUS code, which relies on the radiative transfer code Turbospectrum (Alvarez & Plez 1998; Plez 2012) and the MARCS model atmosphere grid (Gustafsson et al. 2008). The abundance of each chemical species is computed as follows: (*a*) A synthesis is performed, using the full set of atomic and molecular line lists described in Shetrone et al. (2015), Hasselquist et al. (2016), Cunha et al. (2017), and Smith et al. (2021). This set of lists is internally labeled as linelist.20170418 based on the date of creation in the format YYYYMMDD. This is used to find the local continuum level via a linear fit; (*b*) Cosmic rays and telluric line rejections are performed; (*c*) The local S/N is estimated; (*d*) A series of flux points contributing to a given absorption line is automatically selected; and (*e*) Abundances are then derived by comparing the observed spectrum with a set of convolved synthetic spectra characterized by different abundances. Then, four different abundance determination methods are used: (*1*) line-profile fitting; (*2*) core line-intensity comparison; (*3*) global goodness-of-fit estimate; and (*4*) equivalent-width comparison. Each diagnostic yields validation flags. Based on these flags, a decision tree then rejects or accepts each estimate, keeping the best-fit abundance. Here, we adopted the χ^2 diagnostic as the abundance because it is the most robust. However, we store the information from the other diagnostics, including the standard deviation between all four methods.

As described in Fernández-Trincado et al. (2019b), a mix of heavily CN-cycled and α-poor MARCS models were used, as well as the same molecular lines adopted by (Smith et al. 2013), and employed to determine the C, N, and O abundances. In addition, we have adopted the C, N, and O abundances that satisfy the fitting of all molecular lines consistently. We first derive ¹⁶O abundances from ¹⁶OH lines, then derive ¹²C from ¹²C¹⁶O lines, and ¹⁴N from ¹²C¹⁴N lines; the CNO abundances are derived several times iteratively to minimize the OH, CO, and CN de-

pendences. The resulting elemental abundances are provided in the next section.

4.2. Photometric and Spectroscopic Parameters

We also applied a simple approach of fixing T_{eff} and log g to values determined independently of spectroscopy. In order to get T_{eff} and log g from photometry, we compared the differential reddening corrected G_0 vs. $(G_{BP} − G_{RP})_0$ CMD of Fig. 1 with isochrones obtained from the PARSEC database (Bressan et al. 2012). We used a preferred (see Section 6) age of 11.6 Gyrs and a global metallicity calculated taking both [Fe/H] and α-enhancement according to the equation of Salaris et al. (1993). [Fe/H] and α-enhancement were obtained from the BACCHUS measurements. We got the best fit to the RGB using a distance of ∼8.6 kpc and an absorption A$_V$=2.5. After that, we projected horizontally the position of each star until it intersected the isochrone and assumed T_{eff} and log g to be the temperature and gravity of the point of the isochrones that have the same G magnitude of the star. We underline the fact that for highly reddened objects like FSR 1758 the absorption correction depends on the spectral energy distribution of the star, i.e. on its temperature. For this reason we applied a temperature-dependent absortion correction to the isochrone. Without this trick, it is not possbile to obtain a proper fit of the RGB, expecially of the upper and cooler part. The adopted stellar parameters are listed in Table 2.

In Figure 2, we compare the sensitivity to the derived atmospheric parameters, depending on the species and line in question. When the spectroscopic and photometry-based atmospheric parameters were adopted, we found discrepancies in the effective temperature of the order of ∼ 18 − 360 K, and surface gravity differences between $\gtrsim$ 0.09 − 0.5 dex. The larger uncertainties are found mostly for stars in our sample with a lower S/N spectrum, and particularly for hotter ($\gtrsim$ 4500 K) stars. This issue does not strongly affect the derived [X/Fe] abundance ratios, but some chemical species such as carbon, nitrogen, oxygen, and titanium are more sensitive to these discrepancies in the lower S/N regime. It is important to note that these discrepancies do not have a large impact on our conclusions.

5. Elemental abundances

We limit our discussion to [X/Fe] and [Fe/H] abundance ratios obtained from a line-by-line inspection of the APOGEE-2 spectra with the BACCHUS pipeline (Masseron et al. 2016) – independent of ASPCAP, in order to reduce a number of problems produced by the blind ASPCAP processing in lower-metallicity cluster stars (see, e.g., Masseron et al. 2019; Mészáros et al. 2020).

Ten chemical species were investigated from the APOGEE-2 spectra, including the Fe-peak (Fe, Ni), α- (O, Mg, Si, Ca, Ti), light- (C, N), and odd-Z (Al) elements. Our study provides complementary information on elements not accessible from Villanova et al. (2019), therefore C, N, and Si are reported for the first time. The BACCHUS elemental abundances are listed in Table 2 highlighting the mean value of each chemical specie in FSR 1758 from different methods. Internal errors were derived using sensitivities of the abundances to variations in the adopted atmospheric parameters, and the internal uncertainties in each parameter as estimated in Fernández-Trincado et al. (2020a).

This study now places our chemical understanding of FSR 1758 alongside that of other well-studied intermediate-metallicity GCs. Overall, the results for FSR 1758 are in agreement with other GCs of similar metallicity for all species, as shown in Figure 3(a).

Table 2. BACCHUS elemental abundances of the observed stars. The median and mean abundances, and 1σ error are shown for the whole sample. BACCHUS results by adopting photometric and spectroscopic atmospheric parameters are presented in the 30 first lines of the table, which are compared to ASPCAP DR17 and literature results at the end of the table. All the listed elemental abundances have been scaled to the Solar reference from Asplund et al. (2005).

APOGEE-ID	S/N pixel^{-1}	[M/H]	T_{eff} K	log g cgs	ξ_t km s^{-1}	[C/Fe]	[N/Fe]	[O/Fe]	[Mg/Fe]	[Al/Fe]	[Si/Fe]	[Ca/Fe]	[Ti/Fe]	[Fe/H]	[Ni/Fe]
Photometry															
2M17314970−3956247	250	−1.31	4159	0.53	2.69	−0.59	+1.36	+0.51	+0.15	+0.54	+0.25	+0.34	+0.34	−1.32	+0.02
2M17305424−3950496	172	−1.34	4300	0.80	2.07	...	+1.28	+0.33	+0.40	+0.16	+0.35	+0.22	+0.22	−1.38	+0.03
2M17310731−3953523	126	−1.39	4506	1.18	1.71	−0.33	+0.96	+0.77	+0.46	+0.20	+0.32	+0.31	+0.45	−1.22	+0.01
2M17310187−3950066	118	−1.38	4588	1.33	1.90	−0.43	+1.22	+0.64	+0.53	+0.35	+0.30	+0.26	+0.36	−1.29	+0.01
2M17314263−3947053	110	−1.70	4571	1.29	1.35	−0.20	+0.67	+0.56	+0.33	−0.02	+0.44	+0.45	−0.11	−1.61	−0.09
2M17312661−3951342	93	−1.41	4675	1.49	1.79	−0.19	...	+0.78	+0.42	+0.01	+0.31	+0.41	+0.46	−1.26	+0.06
2M17310738−3952298	82	−1.31	4653	1.45	1.68	−0.80	+1.61	+0.46	+0.45	+0.85	+0.33	+0.31	+0.39	−1.35	+0.04
2M17311707−3950382	75	−1.34	4742	1.62	1.81	−0.12	+1.10	+0.68	+0.50	+0.25	+0.29	+0.36	+0.42	−1.29	+0.19
2M17313165−3949120	71	−1.43	4715	1.57	1.47	−0.68	...	...	+0.20	+0.41	+0.43	+0.27	+0.28	−1.45	+0.13
2M17311230−3949493	69	−1.58	4572	1.30	1.64	...	+0.75	+0.68	+0.21	−0.02	+0.25	+0.30	+0.68	−1.44	+0.12
2M17310618−3943037	61	−1.54	4839	1.81	1.61	−0.00	+1.04	+0.80	+0.40	−0.02	+0.30	+0.39	+0.25	−1.35	−0.04
Median	...	...	...	...	...	−0.33	+1.11	+0.66	+0.40	+0.20	+0.32	+0.31	+0.36	−1.35	+0.03
Mean	**...**	**...**	**...**	**...**	**...**	**−0.38**	**+1.12**	**+0.63**	**+0.37**	**+0.25**	**+0.33**	**+0.33**	**+0.34**	**−1.36**	**+0.04**
1σ	...	...	...	...	...	0.26	0.26	0.15	0.13	0.24	0.05	0.07	0.11	0.08	0.07
Spectroscopy															
2M17314970−3956247	250	−1.31	4047	0.79	2.66	−0.42	+1.11	+0.25	+0.11	+0.39	+0.35	+0.22	+0.20	−1.33	+0.04
2M17305424−3950496	172	−1.34	4281	1.03	1.92	...	+1.15	+0.27	+0.33	+0.14	+0.42	+0.17	+0.26	−1.36	+0.06
2M17310731−3953523	126	−1.39	4190	1.01	1.69	−0.21	+0.57	+0.31	+0.31	+0.08	+0.44	+0.19	+0.19	−1.35	+0.07
2M17310187−3950066	118	−1.38	4320	1.23	1.72	−0.33	+0.96	+0.29	+0.42	+0.29	+0.43	+0.19	+0.06	−1.39	+0.10
2M17314263−3947053	110	−1.70	4398	0.81	1.63	−0.04	+0.47	+0.41	+0.25	−0.02	+0.45	+0.49	−0.14	−1.73	−0.16
2M17312661−3951342	93	−1.41	4322	1.22	1.58	−0.13	...	+0.32	+0.29	−0.09	+0.44	+0.36	+0.22	−1.41	+0.13
2M17310738−3952298	82	−1.31	4609	1.56	1.62	−0.62	+1.43	+0.32	+0.33	+0.79	+0.38	+0.27	+0.38	−1.36	+0.12
2M17311707−3950382	75	−1.34	4522	1.52	1.83	−0.07	+0.96	+0.48	+0.36	+0.25	+0.40	+0.33	+0.39	−1.38	+0.19
2M17313165−3949120	71	−1.43	4740	1.29	1.47	+0.21	...	...	+0.21	+0.41	+0.44	+0.23	+0.30	−1.43	+0.13
2M17311230−3949493	69	−1.58	4289	1.15	0.85	...	+0.62	+0.20	+0.31	−0.13	+0.37	+0.20	−0.05	−1.50	+0.10
2M17310618−3943037	61	−1.54	4476	1.32	1.49	−0.13	+0.77	+0.34	+0.33	−0.08	+0.36	+0.37	+0.05	−1.52	−0.06
Median	...	...	...	...	...	−0.13	+0.96	+0.32	+0.31	+0.14	+0.42	+0.23	+0.20	−1.39	+0.10
Mean	**...**	**...**	**...**	**...**	**...**	**−0.19**	**+0.89**	**+0.32**	**+0.29**	**+0.18**	**+0.41**	**+0.27**	**+0.17**	**−1.43**	**+0.07**
1σ	...	...	...	...	...	0.17	0.28	0.06	0.05	0.24	0.04	0.09	0.16	0.08	0.07
ASPCAP DR17															
Median	...	...	...	...	...	−0.41	+0.89	+0.35	+0.34	+0.21	+0.27	+0.29	+0.02	−1.38	−0.02
Mean	**...**	**...**	**...**	**...**	**...**	**−0.41**	**+0.71**	**+0.31**	**+0.29**	**+0.18**	**+0.27**	**+0.27**	**−0.01**	**−1.43**	**−0.01**
1σ	...	...	...	...	...	0.12	0.34	0.11	0.07	0.29	0.04	0.05	0.15	0.09	0.05
Villanova et al. (2019)															
Median	...	...	...	...	...	...	...	+0.37	+0.67	+0.44	...	+0.37	+0.33	−1.49	−0.10
Mean	**...**	**...**	**...**	**...**	**...**	**...**	**...**	**+0.32**	**+0.67**	**+0.43**	**...**	**+0.35**	**+0.31**	**−1.53**	**−0.11**
1σ	...	...	...	...	...	...	...	0.08	0.09	0.13	...	0.08	0.06	0.06	0.05

5.1. The iron-peak elements: Fe, and Ni

We found a mean metallicity [Fe/H] = −1.36 and [Fe/H] = −1.43 depending on the adopted atmospheric parameters. This difference in [Fe/H] is smaller that the internal 1σ deviation, 0.08 dex, as listed in Table 2. Furthermore, the results listed in Table 2 reveal there is no significant metallicity spread, which confirms that FSR 1758 is consistent with other GCs at similar metallicity, as seen in Figure 3(a). However, it is important to note that our mean metallicity is on average ∼ 0.10–0.17 dex higher than the mean metallicity ([Fe/H]= −1.53) determined from optical spectra (Villanova et al. 2019), and ∼0.07 higher than ASPCAP DR17 determination when compared to our determinations by adopting photometric parameters. These differences are highlighted in Table 2.

The nature of this discrepancy could be attributed to several different factors. Unfortunately, there are no common stars between these studies. However, we list some possible causes. Different reference solar abundances or atmospheric models could be responsible. Another possible source of systematic differences could be the result of NLTE and/or 3D effects, which are currently not modeled when fitting the APOGEE spectra (see, e.g., Masseron et al. 2019; Mészáros et al. 2020).

As far as the other iron-peak element we studied, nickel (Ni) is on average slightly over-solar ([Ni/Fe]= +0.04 − +0.07) with a relatively small star-to-star [Ni/Fe] spread, <0.07 dex. We find a ⟨[Ni/Fe]⟩ slightly higher (≳ 0.15 dex) than [Ni/Fe] abundance ratios determined in Villanova et al. (2019). The measured [Ni/Fe] abundance ratio in FSR 1758 is at a similar level to that observed in extragalactic environments at similar metallicity as seen in Figure 4.
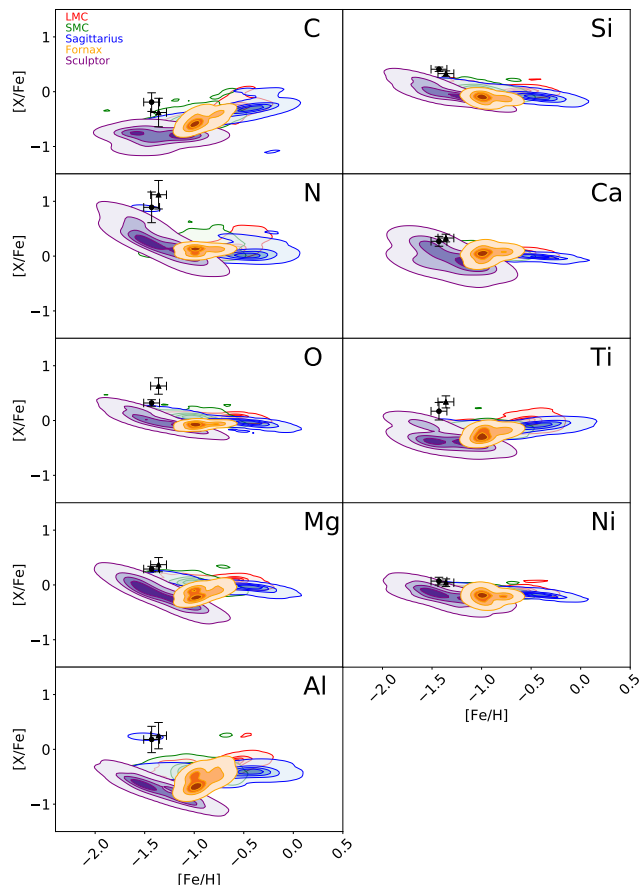
Fig. 4. Kernel Density Estimation (KDE) models of [X/Fe] versus [Fe/H] for star in extragalactic environments, taken from the compilation of stars from Gaia Collaboration et al. (2018b) with ASPCAP DR17 determinations. The black symbols show our BACCHUS elemental abundances determined from spectroscopic (dot symbol) and photometric (triangle symbol) atmospheric parameters.

5.2. The odd-Z elements: Al

We find median values for [Al/Fe] compatible with other Galactic GCs at similar metallicity, as shown in Figure 3(b). The sample has an observed star-to-star spread in [Al/Fe] of $\gtrsim$ +0.8 dex, which greatly exceeds the observational uncertainties. There is at most a weak Al-Mg anti-correlation, possibly showing the signs of a moderate Mg-Al cycle in FSR 1758, common to most intermediate to metal-poor GCs in the Galaxy (Masseron et al. 2019; Mészáros et al. 2020, 2021). Inspection of the [Si/Fe] ratio as a function of [Al/Fe] for the few stars with reliable Si measurements, as shown in Figure 3(d), reveal that there is not a statistically significant correlation between Al and Si, as will be expected from the Mg-Al cycle, as Al-rich stars also present enrichment in Si (see, e.g., Yong et al. 2005; Carretta et al. 2009). Thus, the observed Si-Al trend in Figure 3(d) explains the apparent weak Al-Mg anti-correlation seen in Figure 3(a).

Figure 3(b:e) reveals that, by adopting the rough limit of [Al/Fe]= +0.3 to separate the so-called first- and second-generation stars, as suggested in Mészáros et al. (2020, 2021), there are two apparent groups of stars in FSR 1758. One of these groups, dominated by first-generation stars, exhibits low Al and (slight) Mg enrichment with intermediate N enrichment ([N/Fe]$\lesssim$ 1); while the second group, dominated by second-

generation stars, shows high Al and N enrichment simultaneous with depleted C. Therefore, we conclude that FSR 1758 does indeed host multiple populations common to virtually all GCs, and that in addition to the Na-O anti-correlation identified in Villanova et al. (2019), we also identified the signatures of N-C anti-correlation typical of GCs at similar metallicity. In particular, the presence of a population enriched in [Al/Fe] (> +0.5) in FSR 1758 rules out the possible scenario of FSR 1758 being the nucleus of an accreted dwarf galaxy, since large enrichment in Al has not been observed in dwarf galaxy stellar populations (see, e.g., Shetrone et al. 2003; Hasselquist et al. 2017, 2019).

5.3. The light-elements: C and N

Figures 3(c) and (e) reveal a clear N-C anti-correlation, Al-N correlation, and a large N spread (> +0.9 dex). We conclude that the intra-GC abundance variations reported in Figures 3(c) and (e) are indicative of the presence of multiple populations in FSR 1758. It is the first time that the presence of a spread in C and N has been established in FSR 1758.

5.4. The α-elements: O, Mg, Si, Ca and Ti

Figure 3(a) shows that the α elements in FSR 1758 follow the same trend as other GCs at similar metallicity, again confirming the genuine GC nature of FSR 1758, as originally suggested by Villanova et al. (2019). However, as can be appreciated in Figure 4, the [Ca/Fe] abundance ratio appears to be at the same level as that seen in extragalatic environments.

Finally, Figure 4 reveals that all the chemical species (except [Ni/Fe] and [Ca/Fe]) in our sample depart from the typical level of extragalactic environments, making FSR 1758 unlikely associated with the nucleus of a dwarf galaxy as previously hipothetised in (Barbá et al. 2019). We conclude that the measured elemental abundance ratios and anti-correlation/correlation features support the genuine GC nature of FSR 1758.

6. Age

We estimate the age of FSR 1758 through isochrone fitting. To accomplish this, we employ the SIRIUS code (Souza et al. 2020), which applies a Bayesian statistical inference based on the Markov Chain Monte Carlo method. For the isochrone fitting in the RGB region, we adopt the Darthmouth Stellar Evolutionary Database (DSED: Dotter et al. 2008) with an α-enhancement of +0.4 and canonical helium models of Zero-Age Horizontal Branch (ZAHB) from the Bag of Stellar Tracks and Isochrones (BaSTI: Pietrinferni et al. 2006).

Since we do not have the entire CMD available, in particular the turn-off region, we imposed Gaussian distribution priors for the metallicity of [Fe/H]$\sim$ −1.36 (see Section 5), based on the mean determination from this work, and by assuming an error of ~0.05 dex. Metallicity plays a key role in the morphology of stellar evolutionary models, mainly in temperature (color). Lower metalicities tend to higher temperatures (blue region, see fig. 2 in Souza et al. (2020)). Since the evolutionary stage available in our case is restricted to RGB, we imposed a Gaussian prior in metallicity to limit the permitted values.

Figure 5 presents the best isochrone fitting of the *Gaia* EDR3 CMD. Our fit provides a reasonable solution both in the overplotted isochrone (left panel) and the posterior distributions of the corner plot (right panel). As the best determination to represent the distributions, we adopted the median as the most prob-
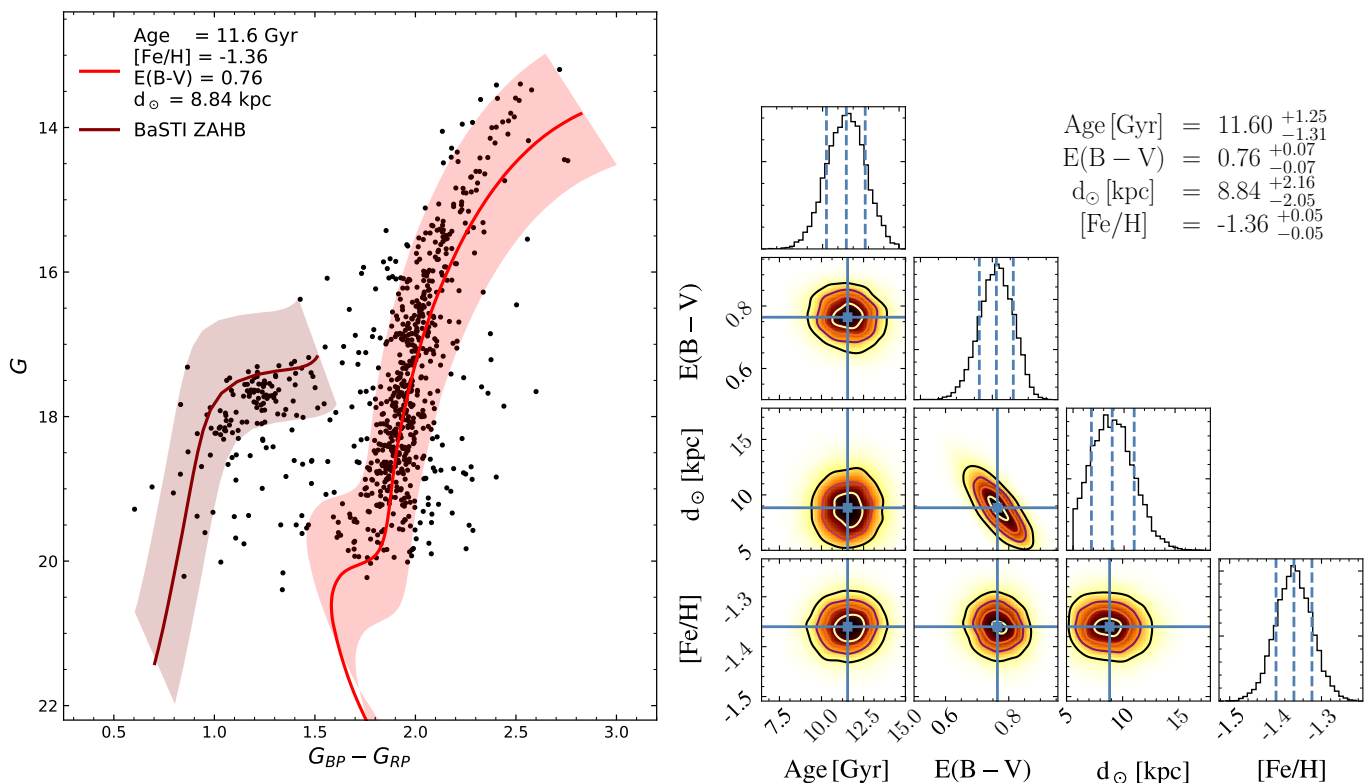
Fig. 5. Age estimation of FSR 1758. Left panel: The best isochrone fit in the *Gaia* bands CMD using DSED models for likely cluster members within 10 arcmin, where the red and brown lines show the most probable solutions, and the shadowed regions indicate the solutions within 1σ. Right panel: The posterior distributions of the indicated quantities.

able value and the uncertainties calculated from 16th and 84th percentiles. A close inspection of the *Gaia* EDR3 CMD reveals that a lower heliocentric distance of $\sim 8.84^{+2.16}_{-2.05}$ kpc better fits the horizontal and RGB simultaneously, with evident large uncertainties likely due to false-positive members located in the red side of the CMD, yielding an age estimate of $\sim 11.6^{+1.25}_{-1.31}$ Gyr for FSR 1758. Suggesting that FSR 1758 is about ~11.6 Gyr old. Clearly, deeper photometry, especially reaching below the MS turnoff, is required to best estimate the age.

The 1σ region (the shaded stripes in Figure 5) is mostly affected by the uncertainties on the distance (vertical) and on the age (horizontal), given our well-determined metallicity. It is relevant to mention that in the RGB region of the CMD, an age variation could be seen as a colour displacement (see Figure 2 of Souza et al. 2020). Also, we want to highlight that our probable solutions within 1σ fit well the central part of the CMD, reinforcing that the age estimation could be a reasonable determination for FSR 1758.

It is also important to note that our detailed analysis yields an estimated reddening of E(B-V)> 0.77, which is 0.4 mag larger than previously estimated by Barbá et al. (2019), E(B−V)~ 0.37. A close inspection of this field show that FSR 1758 is very near to the GCs Tonantzintla 2 (Ton 2; Bica et al. 1996), and NGC 6380 (Ortolani et al. 1998), where the extinction have been found to be as large as E(B−V)~ 1.17 − 1.24 (see, e.g., Bica et al. 1996; Ortolani et al. 1998). This discrepancy could be due to the fact that in Barbá et al. (2019) the 2MASS photometry was employed, which is less sensitive to extinction. Thus, our Bayesian estimation of E(B-V) reveals that FSR 1758 lies in a region with higher reddening, E(B−V)>0.76, than derived by Barbá et al. (2019), which may in fact have been erroneous on the distance

estimation of FSR 1758. This value also appears to be overestimated in Barbá et al. (2019), as confirmed in Figure 5, which shows that a closer distance to FSR 1758 better fits the primary sequences (horizontal branch and RGB) of the cluster.

It is also important to mention, that our estimate distance (8.84 kpc) is in excellent agreement with the mean parallaxes reported by Vasiliev & Baumgardt (2021), 0.119 ±0.011 mas (296 stars), 8.40 kpc. It is important to note that independent methods seem to converge reasonably.

7. Mass

The precise APOGEE-2 *RV* information of our 15 sample stars were combined with other existing *RV* measurements of FSR 1758 members. In particular, Villanova et al. (2019) provided *RV* determinations for nine additional cluster members from optical high-resolution MIKE spectra, while Simpson (2019) reported *RVs* for two additional cluster stars with Gaia radial velocities. This yields a unique collection of 26 likely members of FSR 1758 with *RV* information. With this large sample in hand, we report a mean radial velocity of FSR 1758 of +225.73 ± 0.69 km s^{-1} with a velocity dispersion of 3.51±0.49 km s^{-1}, which is in good agreement with the mean and dispersion reported by Villanova et al. (2019), +226.8 ± 1.6 km s^{-1} and 4.9 ± 1.2 km s^{-1}.

With this relatively large sample of stars with *RV* information, we match the line-of-sight dispersion profiles to the updated version of *N*-body simulations (private communication with H. Baumgardt) of FSR 1758 from Baumgardt & Hilker (2018); Baumgardt et al. (2019), as shown in Figure 6, and thus deter-
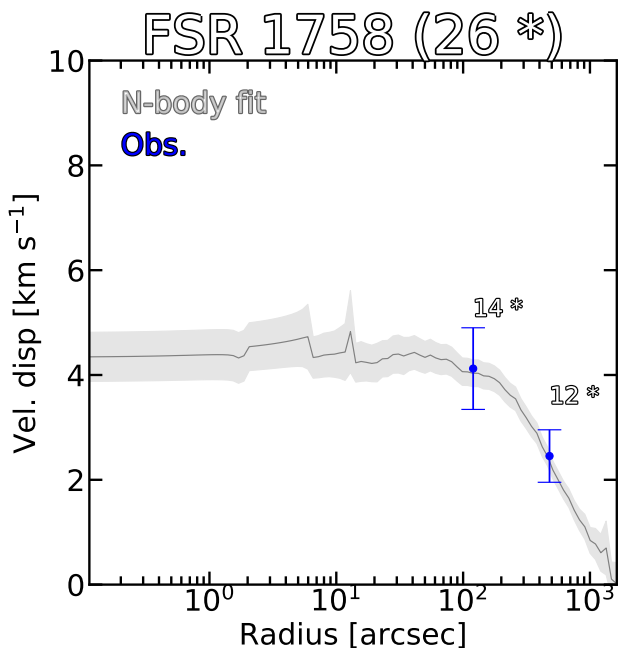
Fig. 6. Line-of-sight velocity dispersion versus radius for our target cluster stars from APOGEE-2 plus Villanova et al. (2019) and Simpson (2019) data set (blue dots). The error bars are refered as $\sigma_{RV}/\sqrt{2 \times N}$. The prediction of the best-fitting updated (private communication) *N*-body model from (Baumgardt & Hilker 2018) and Baumgardt et al. (2019) is shown as a solid-grey line, and the light-grey shaded region indicates the 1σ uncertainty from the fit.

mine the most likely mass of the cluster from kinematic constraints.

We adopted two radial bins (with bin centers of 2′and 8′), chosen to ensure that at least twelve stars were in each bin; resulting in the two points shown in 6. We find $\sigma_0 \sim 4.3 \pm 0.5$ km s^{-1}. This yields a present-day estimated mass of $\sim 2.9 \pm 0.6 \times 10^5$ M$_\odot$, which suggests that FSR 1758 is as massive as NGC 6752 ($\sim 2.32 \pm 0.003 \times 10^5$ M$_\odot$) (Baumgardt & Hilker 2018; Baumgardt et al. 2019).

8. Orbital parameters of FSR 1758

The orbit of FSR 1758 has been extensively discussed in Villanova et al. (2019), Simpson (2019), and Yeh et al. (2020), using different Galactic models. In general, the orbital solutions determined in those studies are consistent, concluding that FSR 1758 is on a highly eccentric and retrograde orbit, with apo-Galacticon <20 kpc and with inner incursions close to the bulge region.

8.1. The Galactic model

Here, we re-visit the orbit of FSR 1758 by adopting the new state-of-the art orbital integration model GravPot16[2] with a "boxy/peanut" bar structure in the bulge region along with other composite stellar components (Fernández-Trincado et al. 2020e), which best fit the known structural and dynamical parameters of our Galaxy, to the best of our knowledge. It is important to note that Villanova et al. (2019) employed the

[2] https://gravpot.utinam.cnrs.fr

GravPot16 model from the web service (https://gravpot.utinam.cnrs.fr) with a simple "prolate" bar structure.

The structural parameters of our bar model (mass, present-day orientation and pattern speed) are 1.1×10^{10} M$_\odot$ (Fernández-Trincado et al. 2020e), 20° (Rodriguez-Fernandez & Combes 2008; Fernández-Trincado et al. 2020e), and 41 km s^{-1} kpc (Sanders et al. 2019), respectively, consistent with observational estimates. The bar scale lengths are $x_0 = 1.46$ kpc, $y_0 = 0.49$ kpc, and $z_0 = 0.39$ kpc, and the middle region ends at the effective semimajor axis of the bar $Rc = 3.28$ kpc , whose density profile is exactly the same as in Robin et al. (2012).

For reference, the Galactic convention adopted by this work is: $X-$axis oriented toward $l = 0°$ and $b = 0°$, $Y-$axis is oriented toward $l = 90°$ and $b = 0°$, and the disc rotates toward $l = 90°$; the velocity is also oriented in these directions. Following this convention, the Sun's orbital velocity vectors are $[U_\odot, V_\odot, W_\odot] = [11.1, 12.24, 7.25]$ km s^{-1} (Brunthaler et al. 2011). The model has been rescaled to the Sun's galactocentric distance, 8.3 kpc, and the local rotation velocity of 244.5 km s^{-1} (Sofue 2015).

8.2. Orbital Elements

For the computation of Galactic orbits, we have employed a simple Monte Carlo approach and the Runge-Kutta algorithm of seventh to eight order, elaborated by Fehlberg (1968). As input parameters we adopted the following observables: (1) $RV = 225.73$ km s^{-1} (see Section 7); absolute proper motions $\mu_\alpha \cos(\delta) = -2.85$ mas yr^{-1} and $\mu_\delta = 2.47$ mas yr^{-1} (see Section 3); and a range of heliocentric distances from 8.84 kpc (as estimated from our isochrone fits in Section 6) and 11.5 ± 1 kpc from Barbá et al. (2019). The uncertainties in the input data (e.g. α, δ, distance, proper motions and RV errors) were randomly propagated as 1σ variation in a Gaussian Monte Carlo resampling. Thus, we ran ten thousand orbits, computed backwards in time during 3 Gyr. The median value of the orbital elements were found for these 10,000 realizations, with uncertainty ranges given by the 16th and 84th percentile. The resulting orbital elements are listed in Table 3. It is important to note that we list the minimal and maximum value of the z-component of the angular momentum in the inertial frame, since this quantity is not conserved in a model with non-axiymmetric structures like GravPot16. In the case of FSR 1758, $L_{z,min}$ and $L_{z,max}$ are close to each other within the uncertainties, thus confirming the genuine retrograde nature of FSR 1758, as shown on the top-right panel in Figure 7.

Overall, our orbital study based on a different Galactic model configuration than previous studies confirms that FSR 1758 lies in an radial, eccentric, and retrograde halo-like orbit, which circulates across the "bulge /bar" region with relatively high vertical excursions from the Galactic plane, $|Z|_{max} \lesssim 8$ kpc, depending on the adopted heliocentric distance as listed in Table 3.

As noted above, there are several studies of FSR 1758 that have attempted to unveil its origin. For instance, Barbá et al. (2019), Myeong et al. (2019), and Massari et al. (2019) proposed that it is likely part of the Sequoia dwarf galaxy, while Simpson (2019) suggested that FSR 1758 is an intruder from the halo into the inner Galaxy. More recent work by Villanova et al. (2019) and Yeh et al. (2020) suggest that the chemical enrichment, high eccentricity, and retrograde orbital configuration of FSR 1758 is not uncommon among other halo GCs, thus favoring a possible *in situ* origin.

To alleviate this tension, we examine the orbital properties of FSR 1758 within the GravPot16+"boxy/peanut"-bar computational environment. Figures 7 and Figure 8 provide an "Orbital

Energy" map that identifies the main structures of GCs with an accreted and in situ origin, respectively. This diagram provides one of the best dynamical representations of the conserved motion quantities in a non-axisymmetric MW model. These include the plot of the characteristic orbital energy, $(E_{max} + E_{min})/2$, versus the orbital Jacobi constant (E_J), as envisioned by Moreno et al. (2015), with E_{max}, E_{min} the maximum and minimum energies per unit mass along each orbit, and computed with respect to the Galactic inertial frame, while E_J has a constant value in the non-inertial reference frame where the bar is at rest.

8.3. Comparison of the orbital elements of FSR 1758 to other globular clusters

We computed the above quantities for the recent compilation of GCs listed in Vasiliev & Baumgardt (2021), adopting the same Monte Carlo approach as described above. Further, we adopted the same GC classification as presented in Massari et al. (2019) to identify the main structures in our maps, and computed the Kernel Density Estimation (KDE) models for each of the GCs groups belonging to the Main-Disc, Main-Bulge, High-Energy, Low-Energy, Sequoia, Gaia-Enceladus-Sausage, Helmi Stream, and Saggitarius population. The resulting KDE models and the their corresponding structure are presented in Figures 7 and 8. This complementary analysis provides us with important insight into the origin of FSR 1758.

Figures 7 and 8 reveal that FSR 1758 lies in the area of this diagram mostly dominated by populations with retrograde orbits. In this diagram, FSR 1758 is located on the boundary of four main structures, the Gaia-Enceladus-Sausage, Helmi Stream, and Sequoia accretion event, and the structure dominated by High-Energy GCs. However, a close inspection of other orbital elements (the orbital eccentricity, the vertical excursions above the Galactic plane, Z_{max}, and the apo-/peri-galactic distance), as presented in Figures 7 and 8, reveal some significant differences. Figure 8 shows that the orbital elements of the FSR 1758 barely overlap the tail of the distribution of the High-Energy structure, which is mostly dominated by highly eccentric and radial orbits with extremely large vertical excursions above the Galactic plane, making less probable that FSR 1758 belongs to this structure.

Figure 7 shows that the Sagittarius structure is dominated by GCs in highly eccentric and radial orbits with $Z_{max} \gtrsim 10$ kpc, barely overlapped by the orbit of FSR 1758 and far away in the "Orbital Energy" map. The same figure reveals that, depending on the adopted heliocentric distance, FSR 1758 departs relatively far away in the "Orbital Energy" map from the Sequoia structure, and is beyond the tail in the eccentricity–Z_{plane}, and barely overlapping the tail of other orbital elements. In other words, GCs in the Sequoia structure are dominated by mostly highly eccentric orbits with large vertical excursions from the Galactic plane ($\gtrsim 20$ kpc), and also reaching large apogalactocentric distances (> 30 kpc), making FSR 1758 a low-probability candidate for association with the Sequoia accretion event. This is also supported by the very old age estimate provided in Section 6.

In addition, Figure 7 reveals that the Gaia-Enceladus-Sausage structure is more confined to the Galactic plane (< 20 kpc), with apogalactocentric distances within < 30 kpc and eccentricities as low as $e \gtrsim 0.55$). Thus, FSR 1758 exhibits orbital properties overlapping fairly well to all the orbital elements of the Gaia-Enceladus-Sausage structure. Therefore, our analysis favors a possible link of FSR 1758 with the Gaia-Enceladus-Sausage accretion event rather than to the Sequoia structure or any possible *in situ* origin. We conclude that it is possible that

Table 3. Main orbital properties of FSR 1758

$d_\odot = 8.84$ kpc (This work)	
Perigalacticon	1.53 ± 0.72 kpc
Apogalacticon	7.11 ± 1.24 kpc
eccentricity	0.64 ± 0.10 kpc
$|Z|_{max}$	2.71 ± 0.82 kpc
$L_{z,min}$	$0.51 \pm 0.26 \times 10^3$ km s^{-1} kpc
$L_{z,max}$	$0.62 \pm 0.17 \times 10^3$ km s^{-1} kpc
E_J	$-1.76 \pm 0.22 \times 10^5$ km^2 s^2
E_{min}	$-2.09 \pm 0.16 \times 10^5$ km^2 s^2
E_{max}	$-1.88 \pm 0.10 \times 10^5$ km^2 s^2
$d_\odot = 11.5$ kpc (Barbá et al. 2019)	
Perigalacticon	3.45 ± 0.6 kpc
Apogalacticon	14.2 ± 4.7 kpc
eccentricity	0.61 ± 0.04 kpc
$|Z|_{max}$	8.1 ± 3.2 kpc
$L_{z,min}$	$0.12 \pm 0.03 \times 10^3$ km s^{-1} kpc
$L_{z,max}$	$0.13 \pm 0.03 \times 10^3$ km s^{-1} kpc
E_J	$-1.04 \pm 0.28 \times 10^5$ km^2 s^2
E_{min}	$-1.59 \pm 0.18 \times 10^5$ km^2 s^2
E_{max}	$-1.56 \pm 0.14 \times 10^5$ km^2 s^2

FSR 1758 has likely been dynamically ejected into the inner halo of the MW from the Gaia-Enceladus-Sausage dwarf galaxy.

9. Summary and concluding remarks

We have performed the first high-resolution (R~22,000) spectral analysis in the *H*-band of the intriguing GC FSR 1758, which was recently discovered toward the bulge region. We used APOGEE data from the CAPOS survey of fifteen RGB stars which are all very likely members. We also provided a dynamical study of the cluster by adopting the state-of-the-art *GravPot16* Galactic model with a "boxy/peanut" bar structure, and employing newly revised estimation of its parameters, inlcuding PMs, *RV* and distance.

We found a mean metallicity of [Fe/H]= -1.36 and [Fe/H]= -1.43, by adopting photometric and spectroscopic atmospheric parameters for FSR 1758, respectively. This value is somewhat more metal rich than previously reported (see, e.g., Barbá et al. 2019; Villanova et al. 2019), with no evidence for an intrinsic metallicity spread. The mean radial velocity of the cluster, determined from a large sample (26 stars), was found to be $+225.73 \pm 0.69$ km s^{-1} with a velocity dispersion of 3.51 km s^{-1}, and the mean PMs in Gaia EDR3 are found to be $\mu_\alpha \cos(\delta) = -2.85 \pm 0.05$ mas yr^{-1} and $\mu_\delta = 2.47 \pm 0.05$ mas yr^{-1}. These values are in good agreement with the literature within the uncertainties.

We derived detailed abundances for 10 species, several of which were not studied previously. Thus, C, N, and Si abundances are reported for the first time. We found evidence for a C-N anti-correlation and N-Al correlation of the sample analyzed. These signatures of multiple populations support the findings from the Na-O anti-correlation found by Villanova et al. (2019) that this GC displays this phenomenon. All of the evidence, including multiple populations, no metallicity spread, relatively high metallicity and small velocity dispersion, clearly indicate that FSR 1758 is a bonafide GC, and not the remnant nucleus of a dwarf galaxy, as originally speculated by Barbá et al. (2019).
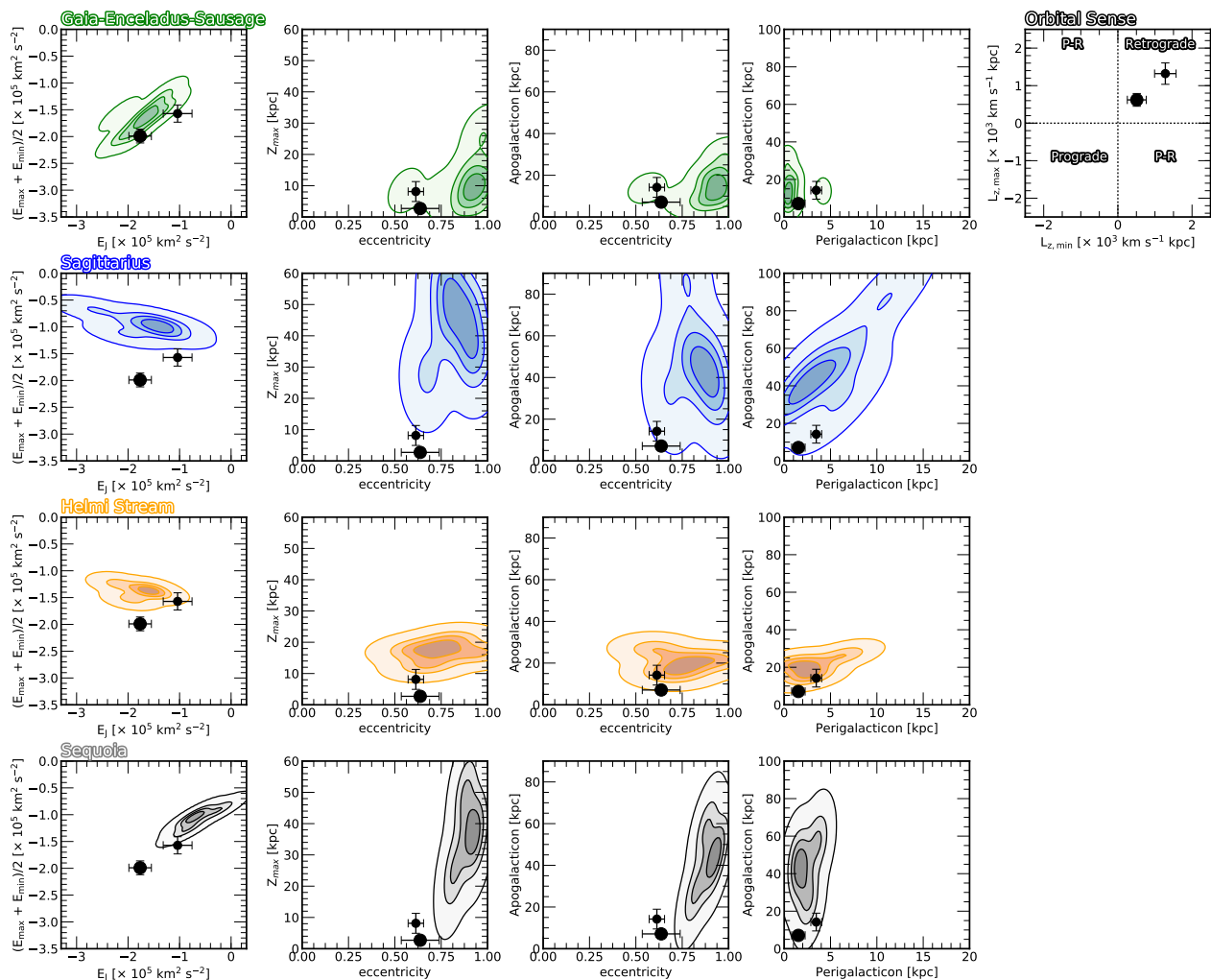
Fig. 7. Kernel Density Estimation (KDE) models of the characteristic orbital energy ((E$_{max}$ + E$_{min}$)/2), the orbital Jacobi energy (E$_J$), orbital pericenter and apocenter, orbital eccentricity, maximum vertical height above the Galactic plane for GCs with an accreted origin (e.g., Massari et al. 2019). FSR 1758 is highlighted with black dot symbols, by considering a heliocentric distance of 8.84 kpc (large symbol), and 11.5 kpc (small symbol) The top-right panel show the minimal and maximum value of the z-component of the angular momentum in the inertial frame, and indicates the regions dominated by prograde and retrograde orbits, and those dominated by orbits that change their sense of motion from prograde to retrograde (P-R).

Note that the suspected tidal tails they noted are now known to be simply outliers in the field star PM distribution. However, this object remains as an outlier in the size vs. Galactocentric distance plot, being very large for a GC so near the center, undoubtedly stemming from the fact that its orbit only brings it this close on occasion.

The SIRIUS code is applied to provide a self-consistent age of FSR 1758 by using a statistical isochrone fitting to the *Gaia* band system. We find that FSR 1758 is as old as $11.6^{+1.25}_{-1.31}$ Gyr.

Additionally, the new dataset was combined with other existing *RV* measurements, allowing a better constraint on the predictions of the *N*-body line-of-sight velocity dispersion of FSR 1758. This yields an estimated mass of $\sim$2.9±0.6 × 10^5 M$_\odot$, which make FSR 1758 as massive as NGC 6752. We also confirm the prevalence of a small velocity dispersion (3.51 ± 0.49 km s^{-1}), which is typical for a GC.

The orbital properties of FSR 1758, combined with its chemical properties and old age estimation, leads to the conclusion that FSR 1758 matches well with the physical properties seen in a good fraction of GCs associated with the Gaia-Enceladus-Sausage accretion event, rather than those associated with the Sequoia event. We favor the association of FSR 1758 with the Gaia-Enceladus-Sausage accretion event, which is also consistent with the age-metallicity relation provided by Massari et al. (2019). Thus, the "Sequoia" GC is not in fact a member of the dwarf galaxy progenitor whose name it inspired (Myeong et al. 2019; Koppelman et al. 2019).
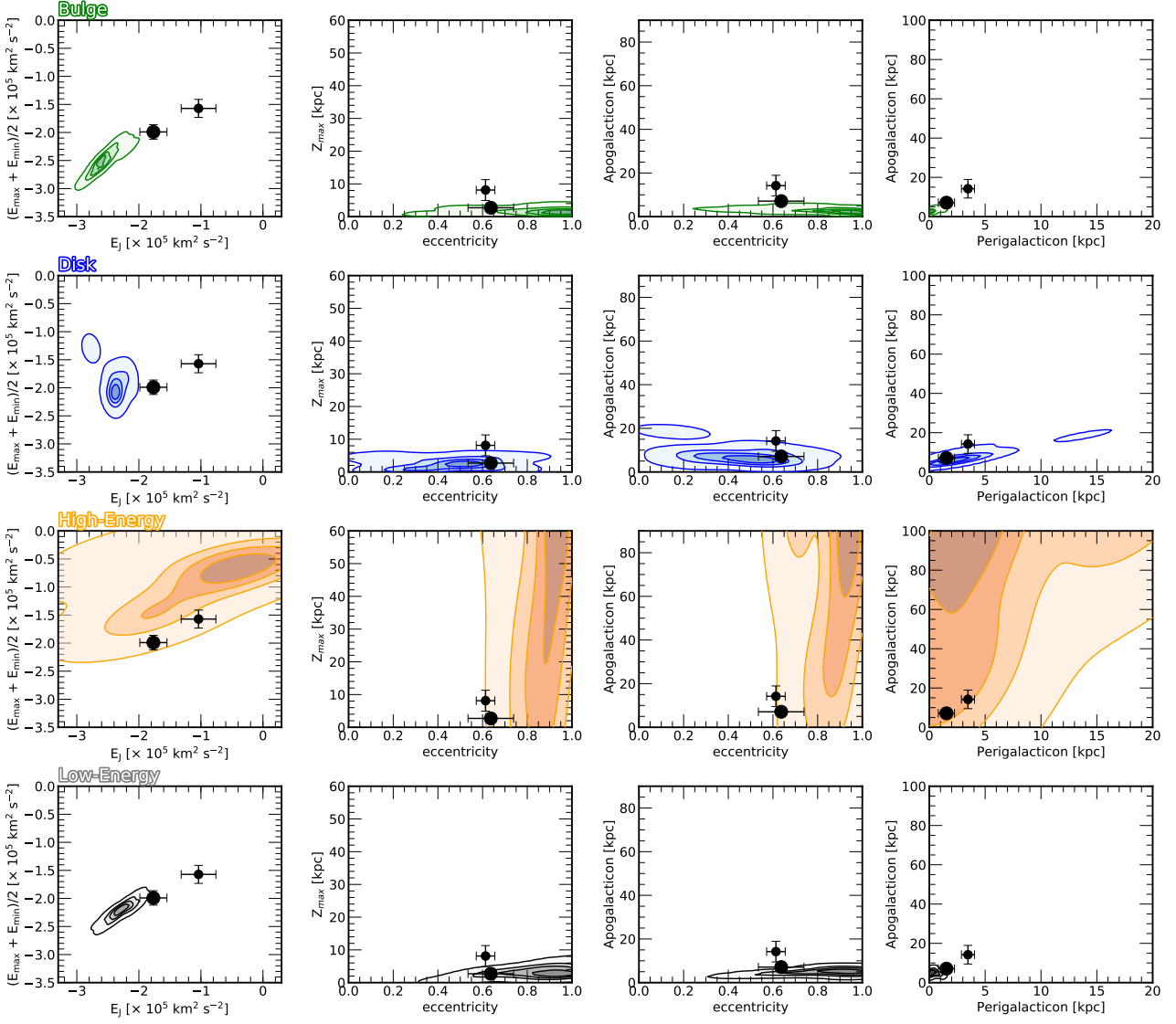
Fig. 8. Same as Figure 7, but now considering GCs with an in situ origin (Massari et al. 2019).

References

Ahumada, R., Allende Prieto, C., Almeida, A., et al. 2020, ApJS, 249, 3
Akaike, H. 1974, IEEE Transactions on Automatic Control, 19, 716
Alonso-García, J., Saito, R. K., Hempel, M., et al. 2018, A&A, 619, A4
Alvarez, R. & Plez, B. 1998, A&A, 330, 1109
Asplund, M., Grevesse, N., & Sauval, A. J. 2005, in Astronomical Society of the Pacific Conference Series, Vol. 336, Cosmic Abundances as Records of Stellar Evolution and Nucleosynthesis, ed. I. Barnes, Thomas G. & F. N. Bash, 25
Barbá, R. H., Minniti, D., Geisler, D., et al. 2019, ApJ, 870, L24
Barbuy, B., Chiappini, C., & Gerhard, O. 2018, ARA&A, 56, 223
Baumgardt, H. & Hilker, M. 2018, MNRAS, 478, 1520
Baumgardt, H., Hilker, M., Sollima, A., & Bellini, A. 2019, MNRAS, 482, 5138
Beaton, R. L., Oelkers, R. J., Hayes, C. R., et al. 2021, ApJ, in preparation
Bica, E., Minniti, D., Bonatto, C., & Hempel, M. 2018, PASA, 35, e025
Bica, E., Ortolani, S., & Barbuy, B. 1996, A&AS, 120, 153
Bica, E., Ortolani, S., & Barbuy, B. 2016, PASA, 33, e028
Blanton, M. R., Bershady, M. A., Abolfathi, B., et al. 2017, AJ, 154, 28
Bowen, I. S. & Vaughan, A. H., J. 1973, Appl. Opt., 12, 1430
Bressan, A., Marigo, P., Girardi, L., et al. 2012, MNRAS, 427, 127
Brunthaler, A., Reid, M. J., Menten, K. M., et al. 2011, Astronomische Nachrichten, 332, 461
Camargo, D. 2018, ApJ, 860, L27
Camargo, D. & Minniti, D. 2019, MNRAS, 484, L90
Cantat-Gaudin, T., Jordi, C., Vallenari, A., et al. 2018, A&A, 618, A93
Cardelli, J. A., Clayton, G. C., & Mathis, J. S. 1989, ApJ, 345, 245
Carretta, E., Bragaglia, A., Gratton, R., & Lucatello, S. 2009, A&A, 505, 139
Contreras Ramos, R., Minniti, D., Fernández-Trincado, J. G., et al. 2018, ApJ, 863, 78
Côté, P. 1999, AJ, 118, 406
Cunha, K., Smith, V. V., Hasselquist, S., et al. 2017, ApJ, 844, 145
Dotter, A., Chaboyer, B., Jevremović, D., et al. 2008, ApJS, 178, 89
Fehlberg, E. 1968, NASA Technical Report, 315
Fernández-Trincado, J. G., Beers, T. C., & Minniti, D. 2020a, A&A, 644, A83
Fernández-Trincado, J. G., Beers, T. C., Minniti, D., et al. 2020b, ApJ, 903, L17
Fernández-Trincado, J. G., Beers, T. C., Minniti, D., et al. 2021a, A&A, 647, A64
Fernández-Trincado, J. G., Beers, T. C., Minniti, D., et al. 2021b, A&A, 648, A70
Fernández-Trincado, J. G., Beers, T. C., Minniti, D., et al. 2020c, A&A, 643, L4
Fernández-Trincado, J. G., Beers, T. C., Minniti, D., et al. 2020d, A&A, 643, L4
Fernández-Trincado, J. G., Beers, T. C., Placco, V. M., et al. 2019a, ApJ, 886, L8
Fernández-Trincado, J. G., Beers, T. C., Tang, B., et al. 2019b, MNRAS, 488, 2864
Fernández-Trincado, J. G., Chaves-Velasquez, L., Pérez-Villegas, A., et al. 2020e, MNRAS, 495, 4113
Fernández-Trincado, J. G., Minniti, D., Beers, T. C., et al. 2020f, A&A, 643, A145
Fernández-Trincado, J. G., Minniti, D., Souza, S. O., et al. 2021c, ApJ, 908, L42
Fernández-Trincado, J. G., Zamora, O., Souto, D., et al. 2019c, A&A, 627, A178
Froebrich, D., Scholz, A., & Raftery, C. L. 2007, MNRAS, 374, 399
Gaia Collaboration, Brown, A. G. A., Vallenari, A., et al. 2018a, A&A, 616, A1
Gaia Collaboration, Brown, A. G. A., Vallenari, A., et al. 2021, A&A, 649, A1
Gaia Collaboration, Helmi, A., van Leeuwen, F., et al. 2018b, A&A, 616, A12
García Pérez, A. E., Allende Prieto, C., Holtzman, J. A., et al. 2016, AJ, 151, 144
Garro, E. R., Minniti, D., Gómez, M., et al. 2021, arXiv e-prints, arXiv:2103.03592
Geisler, D., Villanova, S., O'Connell, J. E., et al. 2021, A&A, submitted
Gran, F., Zoccali, M., Contreras Ramos, R., et al. 2019, A&A, 628, A45
Gunn, J. E., Siegmund, W. A., Mannery, E. J., et al. 2006, AJ, 131, 2332
Gustafsson, B., Edvardsson, B., Eriksson, K., et al. 2008, A&A, 486, 951
Hasselquist, S., Carlin, J. L., Holtzman, J. A., et al. 2019, ApJ, 872, 58
Hasselquist, S., Shetrone, M., Cunha, K., et al. 2016, ApJ, 833, 81
Hasselquist, S., Shetrone, M., Smith, V., et al. 2017, ApJ, 845, 162
Holtzman, J. A., Hasselquist, S., Shetrone, M., et al. 2018, AJ, 156, 125
Jönsson, H., Allende Prieto, C., Holtzman, J. A., et al. 2018, AJ, 156, 126
Jönsson, H., Holtzman, J. A., Allende Prieto, C., et al. 2020, AJ, 160, 120
Kharchenko, N. V., Piskunov, A. E., Schilbach, E., Röser, S., & Scholz, R. D. 2013, A&A, 558, A53

Koppelman, H. H., Helmi, A., Massari, D., Price-Whelan, A. M., & Starkenburg, T. K. 2019, A&A, 631, L9
Kruijssen, J. M. D., Pfeffer, J. L., Reina-Campos, M., Crain, R. A., & Bastian, N. 2019, MNRAS, 486, 3180
Kundu, R., Fernández-Trincado, J. G., Minniti, D., et al. 2019, MNRAS, 489, 4565
Kundu, R., Navarrete, C., Fernández-Trincado, J. G., et al. 2021, A&A, 645, A116
Lindegren, L., Hernández, J., Bombrun, A., et al. 2018, A&A, 616, A2
Majewski, S. R., Schiavon, R. P., Frinchaboy, P. M., et al. 2017, AJ, 154, 94
Massari, D., Koppelman, H. H., & Helmi, A. 2019, A&A, 630, L4
Masseron, T., García-Hernández, D. A., Mészáros, S., et al. 2019, A&A, 622, A191
Masseron, T., Merle, T., & Hawkins, K. 2016, BACCHUS: Brussels Automatic Code for Characterizing High accUracy Spectra
Mészáros, S., Masseron, T., Fernández-Trincado, J. G., et al. 2021, MNRAS[arXiv:2104.12075]
Mészáros, S., Masseron, T., García-Hernández, D. A., et al. 2020, MNRAS, 492, 1641
Minniti, D. 1995, AJ, 109, 1663
Minniti, D., Alonso-García, J., Borissova, J., et al. 2019, Research Notes of the American Astronomical Society, 3, 101
Minniti, D., Alonso-García, J., & Pullen, J. 2017a, Research Notes of the American Astronomical Society, 1, 54
Minniti, D., Fernández-Trincado, J. G., Ripepi, V., et al. 2018a, ApJ, 869, L10
Minniti, D., Geisler, D., Alonso-García, J., et al. 2017b, ApJ, 849, L24
Minniti, D., Gómez, M., Pullen, J. B., et al. 2020, Research Notes of the American Astronomical Society, 4, 218
Minniti, D., Lucas, P. W., Emerson, J. P., et al. 2010, New A, 15, 433
Minniti, D., Palma, T., Dékány, I., et al. 2017c, ApJ, 838, L14
Minniti, D., Ripepi, V., Fernández-Trincado, J. G., et al. 2021, A&A, 647, L4
Minniti, D., Saito, R. K., Gonzalez, O. A., et al. 2018b, A&A, 616, A26
Minniti, D., Schlafly, E. F., Palma, T., et al. 2018c, ApJ, 866, 12
Moreno, E., Pichardo, B., & Schuster, W. J. 2015, MNRAS, 451, 705
Muñoz, C., Geisler, D., Villanova, S., et al. 2018, A&A, 620, A96
Myeong, G. C., Vasiliev, E., Iorio, G., Evans, N. W., & Belokurov, V. 2019, MNRAS, 488, 1235
Nidever, D. L., Holtzman, J. A., Allende Prieto, C., et al. 2015, AJ, 150, 173
O'Donnell, J. E. 1994, ApJ, 422, 158
Ortolani, S., Bica, E., & Barbuy, B. 1998, A&AS, 127, 471
Palma, T., Minniti, D., Alonso-García, J., et al. 2019, MNRAS, 487, 3140
Pérez-Villegas, A., Barbuy, B., Kerber, L. O., et al. 2020, MNRAS, 491, 3251
Pietrinferni, A., Cassisi, S., Salaris, M., & Castelli, F. 2006, ApJ, 642, 797
Plez, B. 2012, Turbospectrum: Code for spectral synthesis, Astrophysics Source Code Library
Recio-Blanco, A., Rojas-Arriagada, A., de Laverny, P., et al. 2017, A&A, 602, L14
Robin, A. C., Marshall, D. J., Schultheis, M., & Reylé, C. 2012, A&A, 538, A106
Rodriguez-Fernandez, N. J. & Combes, F. 2008, A&A, 489, 115
Ryu, J. & Lee, M. G. 2018, ApJ, 863, L38
Saito, R. K., Hempel, M., Minniti, D., et al. 2012, A&A, 537, A107
Salaris, M., Chieffi, A., & Straniero, O. 1993, ApJ, 414, 580
Sanders, J. L., Smith, L., & Evans, N. W. 2019, MNRAS, 488, 4552
Santana, F. A., Beaton, R. L., Covey, K., et al. 2021, ApJ, in preparation
Schlafly, E. F., Green, G. M., Lang, D., et al. 2018, ApJS, 234, 39
Schwarz, G. 1978, Annals of Statistics, 6, 461
Shetrone, M., Bizyaev, D., Lawler, J. E., et al. 2015, ApJS, 221, 24
Shetrone, M., Venn, K. A., Tolstoy, E., et al. 2003, AJ, 125, 684
Simpson, J. D. 2019, MNRAS, 488, 253
Smith, V. V., Bizyaev, D., Cunha, K., et al. 2021, arXiv e-prints, arXiv:2103.10112
Smith, V. V., Cunha, K., Shetrone, M. D., et al. 2013, ApJ, 765, 16
Sofue, Y. 2015, PASJ, 67, 75
Souza, S. O., Kerber, L. O., Barbuy, B., et al. 2020, ApJ, 890, 38
Vasiliev, E. & Baumgardt, H. 2021, arXiv e-prints, arXiv:2102.09568
Villanova, S., Monaco, L., Geisler, D., et al. 2019, ApJ, 882, 174
Wilson, J. C., Hearty, F. R., Skrutskie, M. F., et al. 2019, PASP, 131, 055001
Yeh, F.-C., Carraro, G., Korchagin, V. I., Pianta, C., & Ortolani, S. 2020, A&A, 635, A125
Yong, D., Grundahl, F., Nissen, P. E., Jensen, H. R., & Lambert, D. L. 2005, A&A, 438, 875
Zamora, O., García-Hernández, D. A., Allende Prieto, C., et al. 2015, AJ, 149, 181
Zasowski, G., Cohen, R. E., Chojnowski, S. D., et al. 2017, AJ, 154, 198

1 Centro de Astronomía (CITEVA), Universidad de Antofagasta, Av. Angamos 601, Antofagasta, Chile

2 Instituto de Astronomía y Ciencias Planetarias, Universidad de Atacama, Copayapu 485, Copiapó, Chile

3 Departamento de Astronomía, Casilla 160-C, Universidad de Concepción, Concepción, Chile

4 Departamento de Astronomía, Universidad de La Serena, 1700000 La Serena, Chile

5 Instituto de Investigación Multidisciplinario en Ciencia y Tecnología, Universidad de La Serena. Benavente 980, La Serena, Chile

6 Universidade de São Paulo, IAG, Rua do Matão 1226, Cidade Universitária, São Paulo 05508-900, Brazil

7 Depto. de Cs. Físicas, Facultad de Ciencias Exactas, Universidad Andrés Bello, Av. Fernández Concha 700, Las Condes, Santiago, Chile

8 Vatican Observatory, V00120 Vatican City State, Italy

9 Department of Physics and JINA Center for the Evolution of the Elements, University of Notre Dame, Notre Dame, IN 46556, USA

10 Instituto de Astronomía, Universidad Católica del Norte, Av. Angamos 0610, Antofagasta, Chile

11 Instituto de Astronomía, Universidad Nacional Autónoma de México, Apdo. Postal 106, 22800 Ensenada, B.C., México

12 Instituto de Astronomía, Universidad Nacional Autónoma de México, Apdo. Postal 70264, México D.F., 04510, México

13 Millennium Institute of Astrophysics , Nuncio Monseñor Sotero Sanz 100, Of. 104, Providencia, Santiago, Chile

14 Space Telescope Science Institute, 3700 San Martin Drive, Baltimore, MD 21218, USA